



Research on dual-functional properties of an improved piezoelectric metamaterial beam for simultaneous vibration suppression and energy harvesting

Xingguo Wang^{1,2} · Lan Wang¹ · Haisheng Shu³ · Lei Zhang¹

Received: 19 April 2022 / Accepted: 5 September 2022 / Published online: 21 September 2022
© The Author(s), under exclusive licence to Springer-Verlag GmbH, DE part of Springer Nature 2022

Abstract

An improved dual-functional piezoelectrical metamaterial beam is constructed to achieve vibration suppression and energy harvesting simultaneously. The local oscillator is created by connecting a shunt inductance circuit to a multilayer piezoelectric patch. In addition, each resonator is linked to an external load resistor, to convert vibration energy into electrical energy. A mathematical model of the vibration control and piezoelectric energy harvesting is developed for the improved piezoelectric metamaterial beam, based on which the vibration reduction and energy harvesting performances of the system are evaluated. The analytical results are then validated using finite element (FE) analysis. The FE simulation results of the vibration control and energy harvesting show good agreements with the counterpart analytical results. Moreover, impedance matching analysis is carried out for the dual-functional performance of the improved piezoelectric metamaterial beam, and the influence of impedance on vibration suppression and energy harvesting performance is obtained. Compared to the conventional piezoelectric metamaterial beam, the improved piezoelectric metamaterial beam can generate a lower frequency resonance bandgap, with the center frequency of the bandgap being depending on the number of piezoelectric patch layers and the stacking mode, and a good power generation performance is achieved in lower frequency bands. Therefore, the dual-functional application of the piezoelectric metamaterial beam is extended to a lower frequency band, with avoiding the disadvantage of conventional piezoelectric metamaterials to reduce the resonant frequency by using large inductance components. Notably, electrical loads for the optimal vibration suppression and energy harvesting performance within the bandgap may require different impedance matching. However, it is found that when the electrical load for the optimal output power within the bandgap is chosen as the design basis, not only can a broadband power generation capacity be realized in the bandgap and the passband under the band-edge effect, but a relatively good vibration suppression performance is observed.

Keywords Piezoelectric metamaterial · Vibration suppression · Energy harvesting · Bandgap · Impedance matching

1 Introduction

Metamaterial has emerged as a new force in the field of wave characteristic control in recent years. It is a type of artificially designed material with a special structure, which has

unique properties that natural materials cannot possess, such as negative refractive index, negative mass density, negative stiffness, and many exhibit exotic physical properties [1–5]. Metamaterial has emerged in the field of energy harvesting in the last past decade, showing great research potential due to their unique properties such as wave-guiding, wave-polymerization, and bandgap [6, 7]. At present, more extensive and in-depth studies in the fields of metamaterials and energy harvesting technologies have been conducted, and certain research results have been obtained [8–15]. In recent years, some scholars have combined metamaterials with energy harvesting technology to further expand and realize the diversification of elastic metamaterials in application fields and adaptability to various occasions, and proposed research on the dual-functional characteristics of

✉ Lan Wang
wanglan707@126.com

¹ College of Mechanical and Electrical Engineering, Harbin Engineering University, Harbin 150001, China

² College of Mechanical and Electrical Engineering, Qiqihar University, Qiqihar 161006, China

³ Department of Electromechanical and Automotive, Chizhou Vocational and Technical College, Anhui 247000, China

metamaterials for vibration control and energy harvesting. The significant feature of metamaterial structures is their ability to generate low-frequency bandgaps, which cause elastic waves in the bandgap range to attenuate or fail to pass through the structure, and the energy is more absorbed by the local oscillator structure. Therefore, an energy harvesting device is introduced into the metamaterial oscillator structure, which is expected to harvest the energy localized in the oscillator. The locally resonant metamaterial structure has numerous resonant elements for energy harvesting, which has structural advantages and is an excellent choice for vibration energy harvesters.

Metamaterial dual-functional research is a new application perspective. The study items are mainly primarily classified as linear and nonlinear metamaterial structures; the primary research fields are vibration suppression and energy harvesting, as well as noise suppression and energy harvesting. In 2017, Hobeck and Inman proposed a unique absorber design referred to as a zigzag beam, which can have a natural frequency an order of magnitude lower than that of a basic cantilever beam of the same scale [16]. The zigzag beams can be designed with an added layer of piezoelectric material, which allows them to harvest significant amounts of electrical power as they suppress vibration of the host structure. Li et al. built a metamaterial plate structure and demonstrated through experiments that when the body wave operates in the bandgap range, the body wave is strongly suppressed and the vibration is attenuated, and the metamaterial's four cantilever oscillators capture the external vibration energy and convert it into the kinetic energy of the cantilever beam, which is then converted into electrical energy via the electromechanical conversion of its integrated piezoelectric element [17]. Hu et al. proposed a dual-functional elastic metamaterial beam structure, mainly discussing the influence law of the number of oscillators and distribution form on vibration suppression and energy harvesting [18]. In 2018, Hu et al. constructed an internally coupled elastic metamaterial beam structure by connecting two adjacent oscillators with springs, based on the traditional distributed metamaterial beam. A comparative analysis is performed with the traditional metamaterial distributed beam structure from the dual functions of vibration suppression and energy harvesting [19]. Zhang et al. proposed an acoustic metamaterial construction with a Helmholtz resonant cavity and an integrated membrane diaphragm. The finite element simulation method and experimental verification demonstrated that the construction can achieve low-frequency sound insulation and energy harvesting dual functions simultaneously [20]. In 2019, Chen et al. constructed a metamaterial structural beam using embedded thin-film mass oscillators, which were studied for vibration suppression and energy harvesting, respectively, and experimentally validated [21]. In 2020, Dwivedi et al. introduced piezoelectric elements

into negative stiffness metamaterials to analyze their dual functions of vibration attenuation and energy harvesting [22]. Anigbogu and Bardaweel presented an electromagnetic metamaterial construction capable of attenuating vibrations while also harvesting energy. Unlike prior dual-functional research, this one uses electromagnetic energy harvesting [23]. In terms of structural domains, the above metamaterial dual-functional investigations fall within the category of linear metamaterials. Previous research has indicated that the incorporation of specific nonlinear elements into metamaterials is predicted to improve the dual-functional performance of metamaterials. Some researchers have done dual-functional research on nonlinear metamaterials to this purpose. In 2019, Zhang et al. proposed a multifunctional lattice sandwich structure consisting of a lattice sandwich beam, a nonlinear energy sink (NES) and a giant magnetostrictive material (GMM) [24]. This structure exhibits excellent self-vibration suppression and aeroelastic energy harvesting performance. Cao et al. introduced piezoelectric elements into quasi-zero stiffness structures to construct a vibration isolator with high static and low dynamic stiffness [25]. The research results show that the system can achieve broadband vibration energy harvesting and has excellent vibration isolation capabilities in the low-frequency vibration range. In 2020, Bukhari and Barry constructed the atomic chain structure of nonlinear metamaterials by introducing nonlinear springs [26]. To obtain further detailed information on the nonlinear wave propagation, the spectro-spatial analysis is used in the numerical simulations. This spectro-spatial analysis can reveal the output voltage distortion due to different types of nonlinearities. The results indicate that a nonlinear chain can enhance energy harvesting through the birth of solitary wave and without degrading the boundary of the bandgap. In 2021, Lu et al. arranged a periodic array of electrical energy harvesters, realized by implanting a rolling-ball with coils into a free-moving spherical magnetic cavity on a beam to create bandgaps for wave isolation and produce electrical energy [27]. Such studies that have been conducted have yielded good results and deepened the understanding of the dual-functional realm of metamaterials. However, it should be emphasized that the majority of these studies have used passive mechanical oscillator designs, and once the structures are defined, the vibration suppression and power generation characteristics will be difficult to alter to meet the requirements.

In recent years, Erturk et al. further introduced electro-mechanical oscillators and proposed the dual-functional research of vibration suppression and energy harvesting of piezoelectric metamaterials [28–30]. The main advantage of this type of electromechanical oscillator structure is that the local resonance frequency can be easily adjusted by the circuit without changing the original matrix structure, which avoids the disadvantage that the bandgap of

the mechanical oscillator cannot be adjusted; in addition, compared with the mechanical oscillator metamaterials, the dual-functional study model of the piezoelectric metamaterials will be simpler without the introduction of additional energy harvesting conversion devices. At present, the research on the dual-functional piezoelectric metamaterials is still in its infancy, and many aspects such as model construction, analysis methods, and the dual-functional interaction mechanism have not been sufficiently studied. For example, in the model, segmented electrodes on the entire piezoelectric patch are frequently used to realize the metamaterial's periodicity, resulting in a large size of the piezoelectric bimorph in the length direction, which then brings the problems of piezoelectric patch fabrication and assembly. In the method, the classical modal analysis method is employed in the procedure, which means that the finite modal order is used to approximate the infinite modal order, and the derived mechanical and electrical quantities are an approximation. In the study of dual-functional properties, the main focus is on the power generation performance within the bandgap, and less attention is paid to the interaction between dual-function. To address these issues, our research team conducted additional early-stage research and built a piezoelectric metamaterial dual-functional beam in the form of segmental piezoelectric patches [31]. The accurate analytical solutions of output voltage and output power of each piezoelectric oscillator are given based on the precise charge integration method and transfer matrix approach. The influence of piezoelectric energy harvesting external circuits on metamaterial band-edge effect and band-edge effect on energy harvesting performance are examined. It should be noted that, while this study yielded some useful results, we discovered that when determining the piezoelectric metamaterial structure, the position of the local resonance bandgap is primarily determined by the inductive element in the external shunt circuit, and if one wishes to obtain the dual-functional characteristics in the lower frequency band, a large inductive element is required, which is also a limitation of conventional methods. Simultaneously, the necessity for impedance matching between output power and vibration attenuation performance needs to be researched further.

To this end, the improved piezoelectric metamaterial structure is further constructed in this paper by introducing the piezoelectric stacking technique, and dual-functional characterizations are analyzed. We show that compared with the existing piezoelectric metamaterial beam, the improved piezoelectric metamaterial beam can achieve the vibration bandgap and energy harvesting performance in a lower frequency band with a smaller inductance element under the same electrical parameters. On this basis, we further reveal the different impedance matching requirements of

the electrical load for optimal vibration suppression performance and energy harvesting performance, and conduct related discussions.

This paper's main structure is as follows. The theoretical analysis is the second section. A detailed analysis of the dual-functional properties of the improved piezoelectric metamaterials is presented, focusing on the effect of the low-frequency bandgap generated by the introduction of piezoelectric stacking technology on the dual-functional performance. The finite element simulation study confirms the algorithm and the dual-functional performance results for the theoretical analysis in the third section. The impedance matching analysis is the fourth section. The load matching requirements for vibration suppression performance and energy harvesting performance are explored separately.

2 Theoretical analysis

By incorporating piezoelectric stacking technology into the conventional single-layer piezoelectric metamaterial beam, a new type of improved piezoelectric metamaterial beam, also known as multilayer piezoelectric metamaterial beam, is constructed. A model of the improved piezoelectric metamaterial beam is shown in Fig. 1. The basic unit is made up of three components: a substrate, a piezoelectric bimorph, and a shunt circuit. The piezoelectric bimorph belongs to the transducer unit, the shunt circuit is the control unit, and the substrate structure is defined as the vibration carrier. The upper and bottom surfaces of the substrate beam are periodically attached with piezoelectric patches, ignoring the influence of the adhesive layer on the structural dynamics. To realize the characteristics of the piezoelectric oscillator, the piezoelectric patch is connected to the external circuit, and all the external shunt circuits adopt the same inductance element L . In addition, to reduce the resonant frequency of the local resonant bandgap, the piezoelectric bimorph is connected in parallel, so the polarization direction of adjacent piezoelectric patches are opposite, and they are separately shunted with the external circuit. For the analysis of the power generation performance of the improved piezoelectric metamaterial beam structure, the load resistance is used in the mathematical modeling process to correlate with the power generator to predict the electrical output under a given excitation. Therefore, it is necessary to connect a load resistor R with the same resistance value to each piezoelectric oscillator based on the original piezoelectric metamaterial beam.

Assuming that the thickness of the piezoelectric patch of the conventional piezoelectric metamaterial beam is d , based on which we give two piezoelectric stacking modes, A-mode and B-mode, respectively. Where,

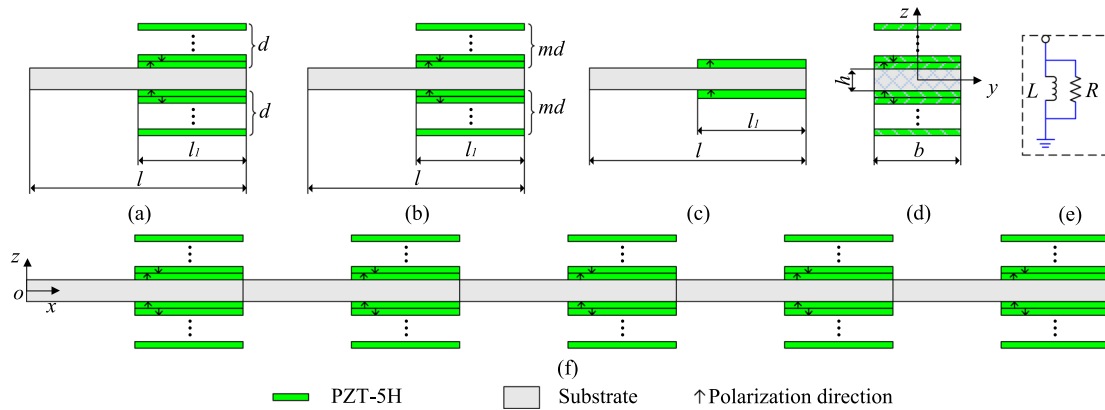


Fig. 1 Model diagram. **a** A-mode basic unit cell; **b** B-mode basic unit cell; **c** conventional mode basic unit cell; **d** cross section; **e** shunt circuit; **f** the finite-length piezoelectric metamaterial beam

A-mode: the number of piezoelectric patch layers is m , the thickness of a single layer is d/m , and the total thickness is d . It is equivalent to dividing the piezoelectric patch by the number of layers (m) based on the conventional piezoelectric metamaterial.

B-mode: the number of piezoelectric patch layers is m , the thickness of a single layer is d , and the total thickness is md . It is equivalent to stacking a piezoelectric patch by the number of layers (m) based on the conventional piezoelectric metamaterial.

A. Vibration suppression of the improved piezoelectric metamaterial beam

This section describes the vibration suppression performance of the improved piezoelectric metamaterial beam through the energy band structure of the infinite periodical model and the vibration transmission characteristics of the finite periodical model.

1. Band structure

For the bending vibration of the beam, the model is simplified to an Euler–Bernoulli beam, whose bending vibration equation is

$$\frac{\partial^2}{\partial x^2} \left[E(x)I(x) \frac{\partial^2 w(x, t)}{\partial x^2} \right] + \rho(x)A(x) \frac{\partial^2 w(x, t)}{\partial t^2} = 0 \tag{1}$$

where ρ, E, A , and I are the density, Young’s modulus, area of the cross section, and moment of inertia of the beam, respectively.

The intrinsic equation of the piezoelectric layer can be expressed as [32]

$$\begin{cases} S_1 = s_{11}^E T_1 + d_{31} E_3 \\ D_3 = d_{31} T_1 + \epsilon_{33}^T E_3 \end{cases} \tag{2}$$

where S_1 and T_1 represent the strain and stress of the piezoelectric patch in the x -direction, respectively; D_3 and E_3

represent the electric displacement and internal electric field of the piezoelectric patch in the z -direction, respectively; s_{11}^E is the elastic compliance coefficient; d_{31} is the strain constant; and ϵ_{33}^T is the constant stress dielectric constant. It has been shown that after the piezoelectric patch is introduced into the external circuit, the positive and negative piezoelectric effects cause the same additional stress T_a to be added to each position of the piezoelectric patch [33].

$$T_a = \begin{cases} \frac{sZd_{31}^2 m^2 b(h+d)}{(s_{11}^E)^2 d(1+sZC_{ps})} \left[\frac{\partial w(l_1, t)}{\partial x} - \frac{\partial w(0, t)}{\partial x} \right] & \text{A - mode} \\ \frac{sZd_{31}^2 mb(h+md)}{(s_{11}^E)^2 d(1+sZC_{ps})} \left[\frac{\partial w(l_1, t)}{\partial x} - \frac{\partial w(0, t)}{\partial x} \right] & \text{B - mode} \end{cases} \tag{3}$$

where C_{ps} denotes the total intrinsic capacitance under the constant strain of the parallel piezoelectric bimorph, Z denotes the impedance of the shunt circuit, and s is the complex variable of Laplace transformation.

$$C_{ps} = \begin{cases} 2m^2 \frac{\epsilon_{33}^s A_s}{d} & \text{A - mode} \\ 2m \frac{\epsilon_{33}^s A_s}{d} & \text{B - mode} \end{cases} \tag{4}$$

where A_s is the area of the electrode and $A_s = bl_1$.

The transfer matrix of the flexural wave propagating in the piezoelectric metamaterial beam has been deduced in detail in the previous research, and instead of repeating it here, the relevant derivation is directly quoted as follows [31]:

$$|\mathbf{T} - e^{ikl}\mathbf{I}| = 0 \tag{5}$$

where \mathbf{T} is the transfer matrix and k is the number of waves. For a given excitation frequency ω , the wave vector k can be derived.

The ideal one-dimensional piezoelectric metamaterial beam structure refers to an infinite period in the x -direction, and the bandgap characteristics are described by the propagation constant of elastic waves in the band structure. In the calculation of the bandgap of the piezoelectric metamaterial beam structure, the structural and material parameters involved are shown in Table 1.

Figure 2 shows the model diagram of the improved piezoelectric oscillator unit with $m=2$. To characterize the energy band behavior of the improved piezoelectric metamaterial beam system itself, here, the load circuit defining energy harvesting is made open-circuit in this case. Based on the combination of charge precise integration method and transfer matrix method, the energy band characteristic curve of the flexural wave propagating in the improved piezoelectric metamaterial beam structure is obtained, as shown in Fig. 3. Figure 3a, b depict to the real and imaginary wave vectors of A-mode, respectively. The energy band curve contains two bandgaps in the range of 390–586 Hz (Bragg bandgap) and 644–658 Hz (local resonance bandgap), and corresponds to the maximum attenuation constant at the resonant frequency (646 Hz) is 0.39. Figure 3c, d depict to the real and imaginary wave vectors of B-mode, respectively. Similarly, the energy band curve of B-mode also contains two bandgaps in the range of 378–580 Hz (Bragg bandgap) and 910–916 Hz

(local resonance bandgap), and the corresponding maximum attenuation constant at the resonant frequency (912 Hz) is 0.70. For comparative analysis, the real and imaginary wave vectors of the conventional piezoelectric metamaterial beam are given in Fig. 3e, f, where 390–594 Hz corresponds to the Bragg bandgap and 1250–1274 Hz corresponds to the local resonance bandgap, with a maximum attenuation constant of 0.83 in the bandgap. Therefore, when compared to the energy band curve of the conventional piezoelectric metamaterial beam, the improved piezoelectric metamaterial's center frequency of the local resonance bandgap is significantly lower for the same electrical parameters, as is the maximum decay constant within the bandgap.

To reveal the specific connection between the resonant frequency of the local oscillator of the improved piezoelectric metamaterial beam and the number of piezoelectric patches layers, stacking mode, and inductance parameters, two sets of parameters are analyzed.

A-mode: specify the total thickness of the piezoelectric patch as d ($d=0.2$ mm), the number of layers m is taken as 1–5 layers, and the thickness of a single layer is d/m .

B-mode: specify the total thickness of the piezoelectric patch as md ($d=0.2$ mm), the number of layers m is taken as 1–5 layers, and the thickness of a single layer is d .

Firstly, the relationship between the resonant frequency of the local oscillator of the improved piezoelectric metamaterial beam and the number of layers and stacking modes of the piezoelectric patch is discussed and analyzed. Table 2 shows the resonant frequency of the local oscillator of improved piezoelectric metamaterial beam versus the number of piezoelectric layers and the stacking mode. As shown in the Table 2, the resonant frequency of the local oscillator gradually decreases with the increase of the number of layers m for the same inductance parameter ($L=65$ mH), where the resonant frequency of the A-mode is approximately $1/m$ of the conventional model, while the resonant frequency of the B-mode is approximately $1/\sqrt{m}$ of the conventional model. Therefore, the improved piezoelectric metamaterials exhibit lower frequency bandgap behavioral properties than conventional metamaterials.

Next, the inductance parameters are analyzed for the piezoelectric metamaterial beam. Table 3 shows the resonant frequency of the local oscillator of conventional and improved piezoelectric metamaterials beams versus the inductance L parameter. The number of layers m of the improved

Table 1 Structural and material parameters of the unit cell of the piezoelectric metamaterial beam

Items	Parameter	Value	Unit
Substrate	Density ρ_1	1142	kg/m ³
	Young's Modulus E	2.0	GPa
	Width b	20	mm
	Thickness h	5	mm
	Periodic constant l	90	mm
PZT-5H	Density ρ_2	7500	kg/m ³
	Elastic compliance coefficient s_{11}^E	1.65*e11	m ³ /N
	Stress dielectric constant e_{33}^T	3.01*e-8	F/m
	Strain constant d_{31}	-2.74*e-10	C/m ²
	Thickness d	0.2	mm
	Length l_1	45	mm
	Layer m	2	
Circuit component	Inductance L	0.065	H

Fig. 2 Basic unit cell model diagram

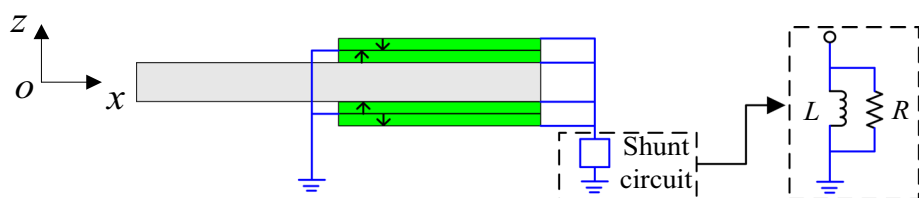


Fig. 3 Flexural wave energy band diagrams of the improved and conventional piezoelectric metamaterial beam: **a, b** A-mode; **c, d** B-mode; **e, f** conventional mode

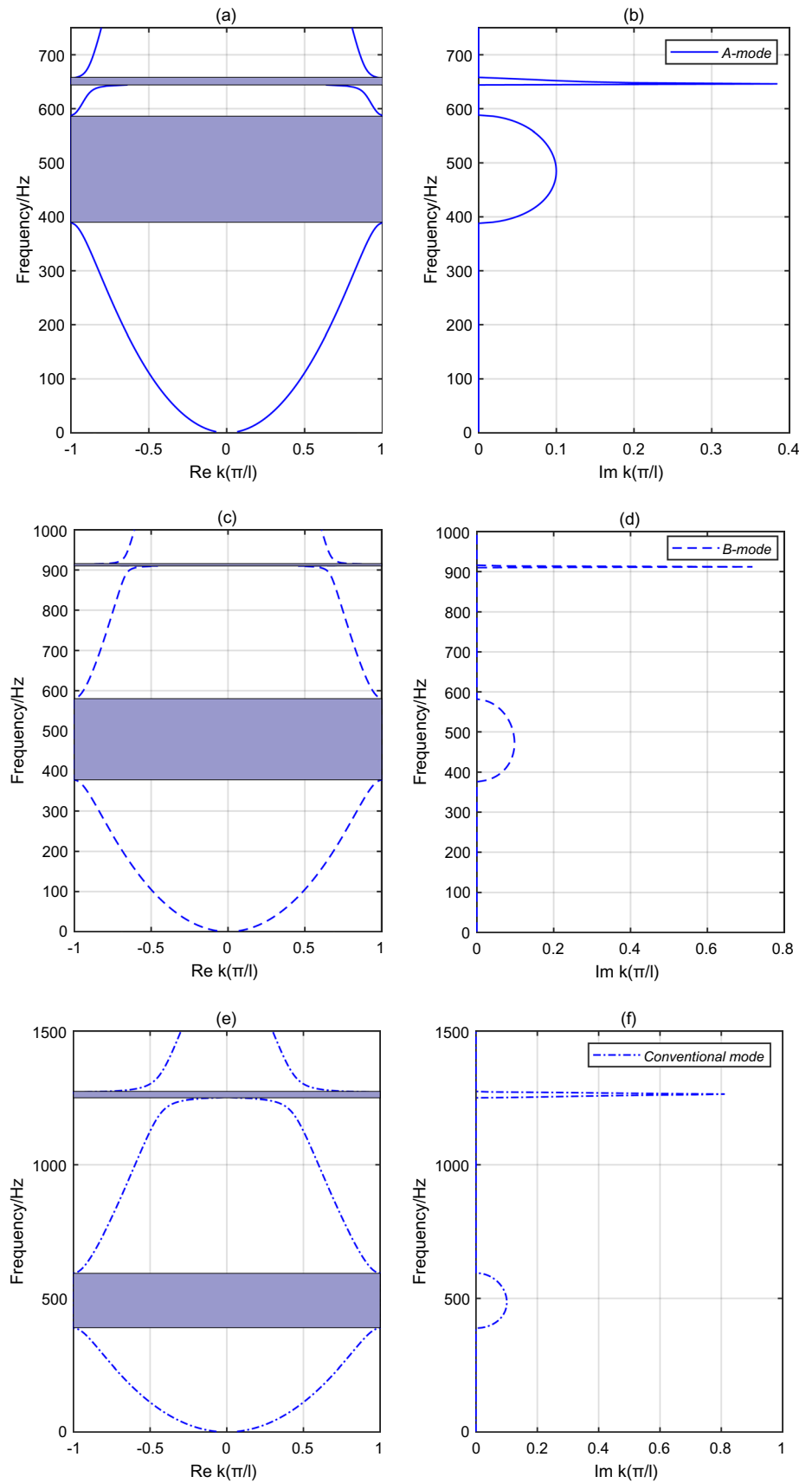


Table 2 The resonant frequency of the local oscillator of improved piezoelectric metamaterial beam versus the number of piezoelectric layers and the stacking mode

<i>m</i>	1	2	3	4	5
A-mode (Hz)	1263	646	433	325	260
B-mode (Hz)	1263	912	743	646	579

metamaterial is 2 and the value range of the inductance parameter *L* is 50–400 mH. It is discovered that, firstly, these three sets of data show a similar pattern of change, with the increasing value of inductance, the resonant frequency of the oscillator continues to decrease, but the slope of this decline is also constantly changing. When the inductance value is small (such as 50–200 mH), increasing the inductance can more obviously reduce the resonant frequency of the oscillator, and when the inductance value is large (such as 200–400 mH), its influence tends to weaken. Second, for the same inductance value, both improved modes can obtain lower resonant frequencies than the conventional mode; for example, for inductance of 200 mH, the conventional mode corresponds to a resonant frequency of 728 Hz, whereas A-mode and B-mode correspond to resonant frequencies of 367 Hz and 520 Hz, respectively, and the percentage of decrease is approximately 50% and 30%, respectively. Finally, for a given resonant frequency, such as 500 Hz, the conventional piezoelectric metamaterial beam requires an inductance of 400 mH, whereas the improved piezoelectric metamaterial requires only 25% (A-mode) or 50% (B-mode) of the conventional model.

Analyzing the influence law of the number of layers, stacking mode, and inductance parameters of the piezoelectric metamaterial beam reveals that the improved piezoelectric metamaterial beams can achieve lower resonant frequency with smaller inductance by selecting the appropriate number of layers and stacking mode.

Next, the effect of introducing an energy harvesting load circuit into a piezoelectric oscillator on vibration suppression of the original piezoelectric metamaterial beam system is analyzed. Here, let the load resistance *R* = 100 kΩ, and the energy band characteristic curves of the flexural wave propagation after the energy harvesting load circuit is introduced into the piezoelectric oscillator unit in the improved A-mode and B-mode and the conventional model, respectively, are shown in Fig. 4. The energy band diagram shows that, similar to the energy band curve in Fig. 3, the Bragg bandgap

and the local resonance bandgap are generated in the entire frequency domain. In the low frequency region, the Bragg bandgap does not change significantly, and the bandgap ranges are 390–586 Hz, 378–580 Hz, and 390–594 Hz, respectively. The results reveal that the Bragg bandgap is mainly caused by the impedance mismatch between the piezoelectric bimorph and the substrate, and that the external circuit has a minor impact.

The local resonance bandgap changes significantly, and the dispersion curve at the band-edge does not display two flat bands. The passband at the upper and lower band-edges also exhibits attenuation performance, with attenuation ranges of around 620–670 Hz, 886–940 Hz, and 1180–1340 Hz, respectively. The maximum attenuation position corresponding to the local resonance bandgap ranges remains unchanged, while the maximum attenuation constant decreases. This indicates that after the introduction of the energy harvesting external load circuit, the improved piezoelectric metamaterial beam exhibits a certain attenuation performance in the passband at the band-edge of the local resonance bandgap, which is equivalent to expanding the scope of the local resonant bandgap while reducing the maximum attenuation within the bandgap.

2. Transmittance

The energy band analysis is based on the fact that elastic waves in the corresponding bandgap will not be propagated under ideal conditions of infinite periods of metamaterials. Elastic waves, on the other hand, will exhibit apparent attenuation within the bandgap in a finite periodic pattern. As a result, the following part investigates a more feasible finite-length model to characterize the vibration control behavior of the improved piezoelectric metamaterials. The bending vibration transmission properties of the improved piezoelectric metamaterial beam in A-mode and B-mode with 20 periods (*m* = 2) are investigated in this paper. The piezoelectric metamaterial's structure and material parameters are set as shown in Table 1, and the external circuit parameters are set in accordance with the energy band analysis.

The transmittance of the system is defined and calculated as

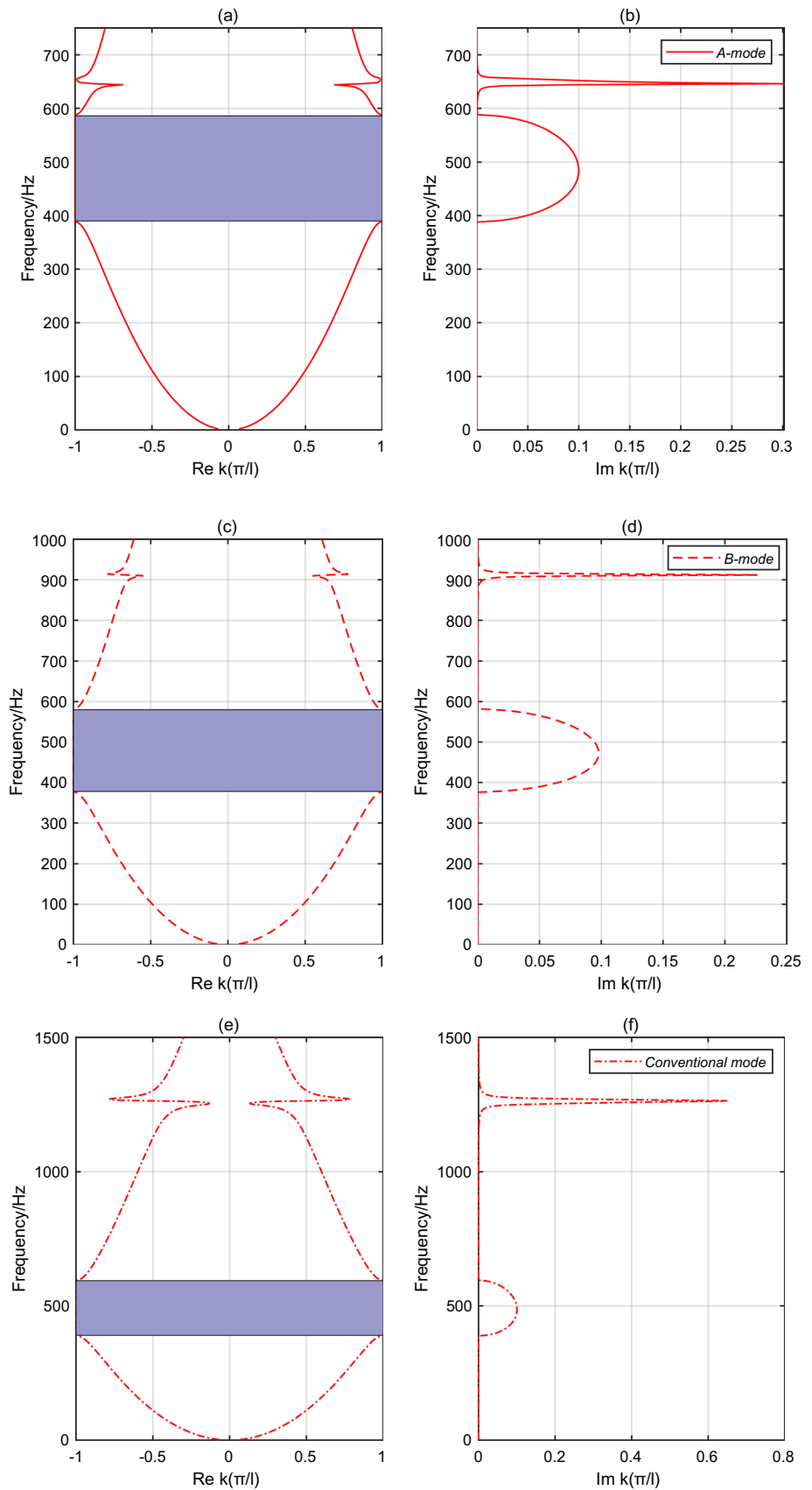
$$\tau = 20 \lg \left(\left| \frac{W_{out}}{W_{in}} \right| \right), \tag{6}$$

where *W_{in}* and *W_{out}* denote the transverse displacement amplitudes of the left-hand input side and the right-hand

Table 3 The resonant frequency of the local oscillator of conventional and improved piezoelectric metamaterials beams versus the inductance parameter

<i>L</i> (mH)	50	100	150	200	250	300	350	400
Conventional mode (Hz)	1442	1017	830	728	642	586	543	507
A-mode (Hz)	736	521	425	367	328	300	278	260
B-mode (Hz)	1040	735	600	520	465	425	393	367

Fig. 4 Flexural wave energy band diagrams of the improved and conventional piezoelectric metamaterial beams after external energy harvesting load circuit: **a, b** A-mode; **c, d** B-mode; **e, f** conventional mode

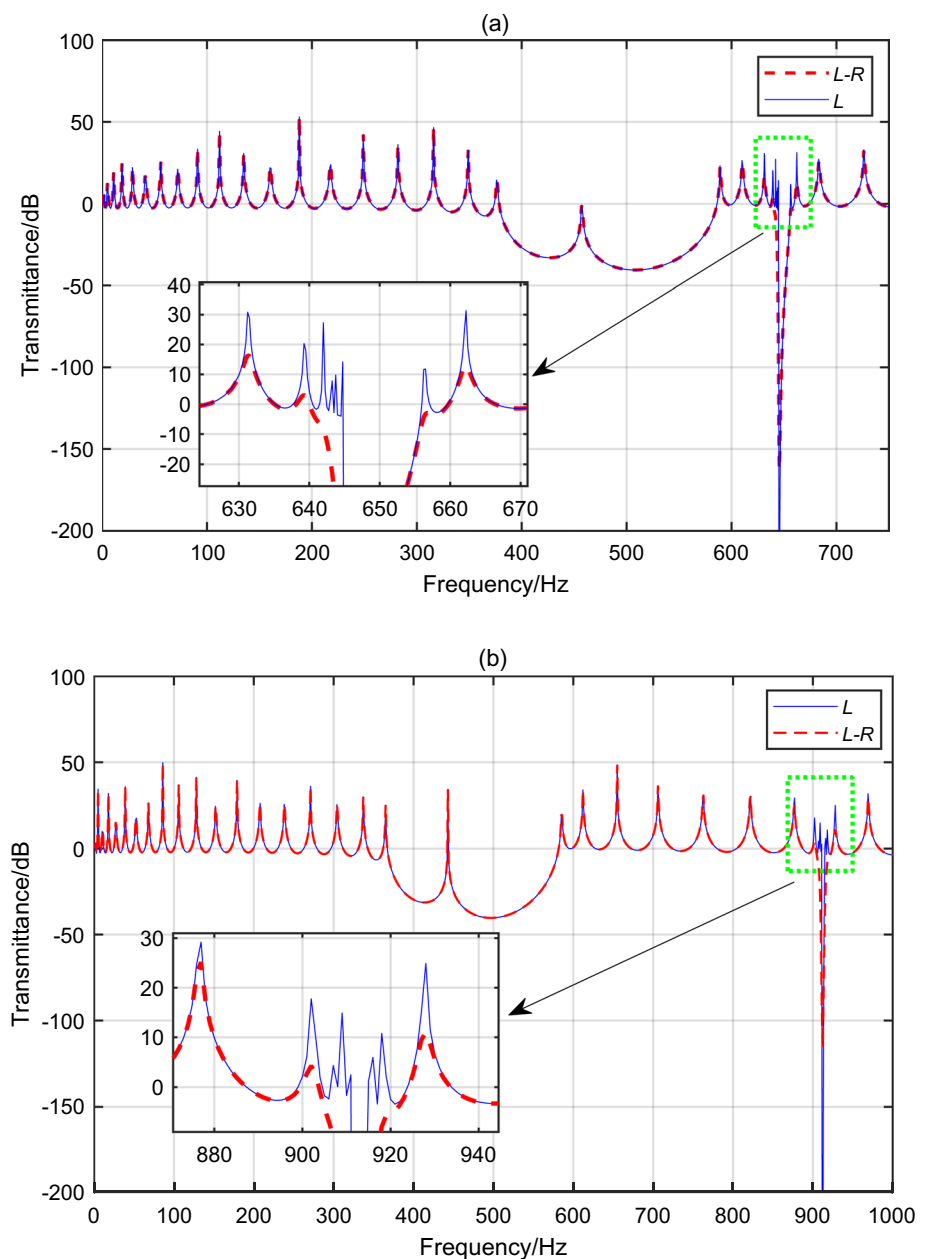


output side of the piezoelectric metamaterial beam system, respectively.

The right-hand end face of the finite structural beam is free boundary, and the left-hand end face is excited with specified transverse displacement along the z -direction with displacement amplitude $W_{in} = 0.01$ mm in the frequency domain of 1–750 Hz (mode A) and 1–1000 Hz (mode B), respectively. The piezoelectric metamaterial beam has certain specified boundary conditions and is modeled based on the Euler–Bernoulli beam theory by assuming geometrically small oscillations and linear-elastic material behavior. For simplicity, the beam is assumed to be undamped, that is, the damping effect of the beam is not considered.

Figure 5a, b show the vibration transmission curves of the 20-period improved piezoelectric metamaterial beam in A-mode and B-mode, respectively. Firstly, when comparing the numerical calculation results of both L and LR modes for the A-mode of Fig. 5a, it is clear that both exhibit Bragg band-gap characteristics at low frequencies (379–587 Hz), and the two vibration transmission curves overlap, indicating that the external energy harvesting load circuit does not significantly change the behavioral characteristics of the Bragg bandgap. The L mode exhibits a local resonance bandgap in the frequency band 644–656 Hz, with a maximum attenuation of around 200 dB within the bandgap. Furthermore, a significant band-edge effect is formed at the bandgap's band-edge,

Fig. 5 Bending vibration transmission curves of the improved piezoelectric metamaterial beam: **a** A-mode; **b** B-mode



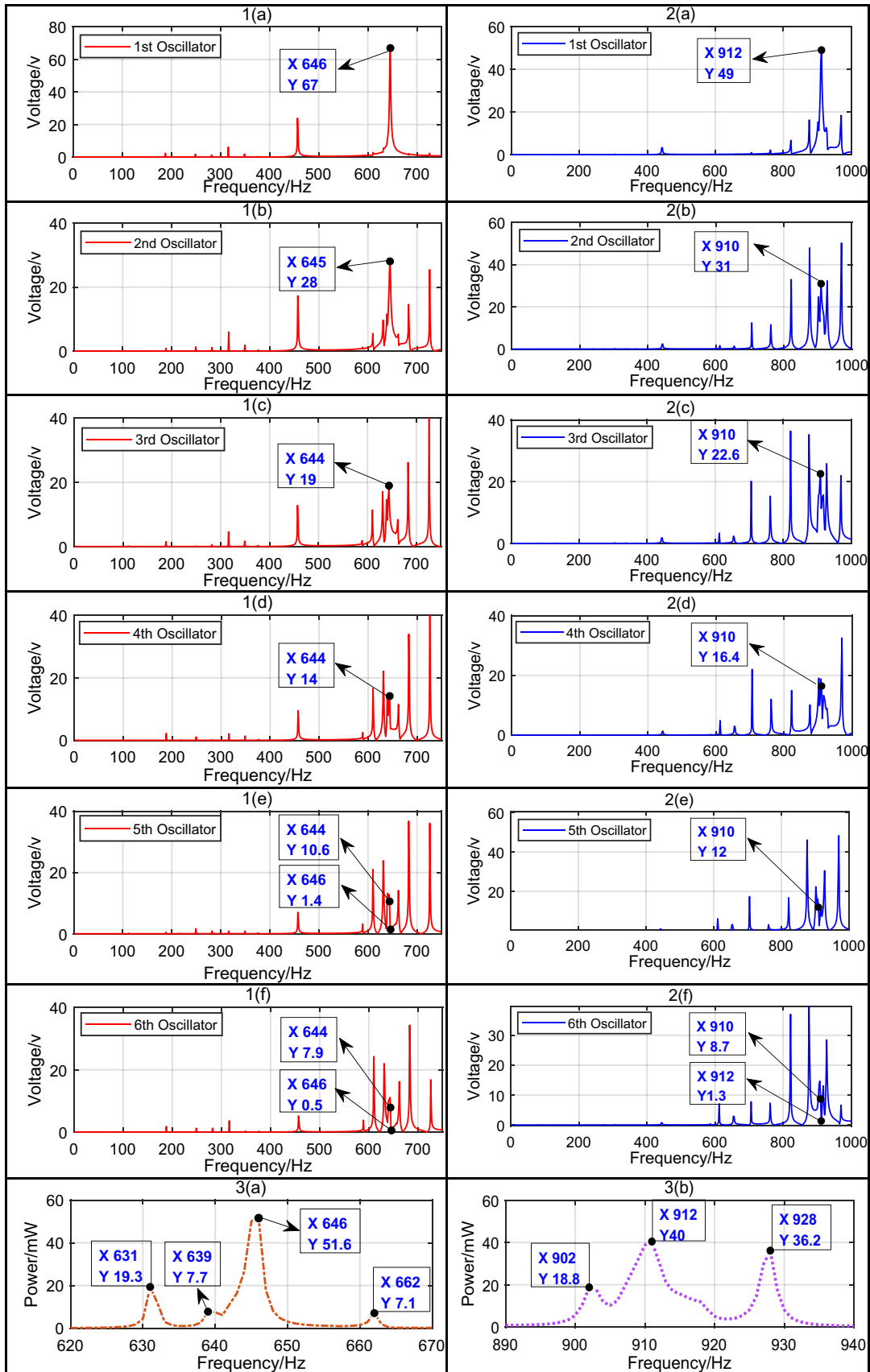


Fig. 6 Output voltages of the 1st–6th oscillators under bending vibration of the improved piezoelectric metamaterial beam: **1a–1f** A-mode, **2a–2f** B-mode; the total output power of the 1st–6th oscillators under the bending vibration of the improved piezoelectric metamaterial beam: **3a** A-mode; **3b** B-mode

where multiple small resonance peaks cluster in the upper and lower band-edge areas. The maximum attenuation in the local resonance bandgap of the piezoelectric metamaterial beam is reduced from 200 to 160 dB when the energy harvesting load circuit is introduced (*LR* mode), indicating that the introduction of the energy harvesting load reduces the maximum attenuation in the local resonance bandgap of the piezoelectric metamaterial beam. It is also worth noting that the band-edge effect is significantly suppressed in the locally expanded image in Fig. 5a. The major symptoms are the elimination of several tiny resonance peaks concentrated in the upper and lower band-edge of the frequency bands 638–644 Hz and 656–659 Hz, as well as a significant attenuation of transmittance corresponding to relatively strong resonance peaks near the band-edge (e.g., 631 Hz, 662 Hz). The numerical calculation results of both the *L* and *LR* modes are likewise provided for the B-mode of Fig. 5b. By examining the vibration transmission curve of B-mode, it is clear that, with the exception of the position, bandwidth, and maximum attenuation of the local resonance bandgap, the rest of the behavioral characteristics are comparable to those of A-mode, which will not be discussed here. To summarize, the vibration transmission characteristics reflected in Fig. 5 are consistent with the energy band characteristics resulting in Figs. 3 and 4.

B. Energy harvesting of the improved piezoelectric metamaterial beam

This section describes the power generation performance of the improved piezoelectric metamaterial beams by the relationship between the output voltage and frequency of each piezoelectric oscillator in the metamaterial, focusing on the relationship between the bandgap characteristics and the band-edge effect of the metamaterial beam and the power generation performance.

According to Kirchoff’s current law, the control equation of the circuit part is:

$$C_{ps} v'(t) + \frac{v(t)}{Z} + \vartheta \left[\frac{\partial^2 w(l_1, t)}{\partial x \partial t} - \frac{\partial^2 w(0, t)}{\partial x \partial t} \right] = 0, \tag{7}$$

where

$$\vartheta = \begin{cases} \frac{d_{31} mb(h + d)}{s_{11}^E} & \text{A - mode} \\ \frac{d_{31} mb(h + md)}{s_{11}^E} & \text{B - mode} \end{cases}. \tag{8}$$

Applying the Laplace transform, we can derive the voltage amplitude of the *n*th period piezoelectric patch

$$V_n = \frac{\vartheta s}{\left(1/Z + sC_{ps}\right)} \left[\frac{\partial W_{n2}(l_1)}{\partial x} - \frac{\partial W_{n2}(0)}{\partial x} \right]. \tag{9}$$

Then the output power P_n of the load resistor R in the external circuit of the *n*th period unit is expressed as:

$$P_n = \frac{V_n^2}{R} = \frac{\left(\frac{\vartheta s}{\left(1/Z + sC_{ps}\right)} \left[\frac{\partial W_{n2}(l_1)}{\partial x} - \frac{\partial W_{n2}(0)}{\partial x} \right] \right)^2}{R}. \tag{10}$$

The right-hand end face of the finite structural beam is free boundary, and the left-hand end face is excited with specified transverse displacement along the *z*-direction with displacement amplitude $W_{in}=0.01$ mm in the frequency domain of 1–750 Hz (mode A) and 1–1000 Hz (mode B), respectively. Figure 6**1a–f** lists the output voltage frequency response curves of the 20-period improved piezoelectric metamaterial beams (A-mode) for the 1st–6th oscillators under the action of bending vibration. Throughout the frequency domain range of 625–665 Hz, the 1st–6th oscillators of the improved piezoelectric metamaterial beam exhibit broadband power generation performance. We concentrate on the aforementioned two frequency bands for power production performance analysis, focusing on the local resonance bandgap and its passband band where the band-edge effect is formed. Firstly, the 1st oscillator has a significant power generation capability within the local resonance bandgap, with a maximum output voltage (67 V) at the resonant frequency (646 Hz). They also show substantial output voltages inside the local resonance bandgap for the 2nd to 6th oscillators, in the order of 28 V, 19 V, 14 V, 10.6 V and 7.9 V. However, the output voltage levels are much lower than those of the 1st oscillator. The reason for this is attributed to the local resonance bandgap characteristic of the metamaterial, i.e., when the excitation frequency is in the local resonance bandgap, the mechanical energy will be localized in the local oscillator. For finite-period structures, this often results in the vast majority of the energy being absorbed by the oscillator near the source. In addition, all the oscillators also exhibit strong power generation performance in the passband at the band-edge. The highest output voltages at the band-edge of the 1st–6th oscillators are 22.9 V, 18.9 V, 14.6 V, 22 V, 12.8 V, and 11 V, in that order. The aforementioned phenomenon corresponds to the vibration suppression analysis of the improved piezoelectric metamaterials. In fact, during the vibration transmission characteristics analysis, we have already investigated the effect of the introducing an external load circuit for energy harvesting on the vibration suppression of the original system, and pointed

out that the modal peaks that generate the band-edge effect are significantly suppressed, resulting in the energy of the modal peaks being absorbed by the piezoelectric oscillator and converted into electrical energy output, so it is easy to understand that the power generation performance here is improved. Similarly, Fig. 62a–f lists the output voltage frequency response curves of the 1st–6th oscillators under the action of bending vibration of the 20-period improved piezoelectric metamaterial beam (B-mode). The output voltage of each oscillator of the improved piezoelectric metamaterial beam (B-mode), like the power production performance of A-mode, is concentrated in the local resonance bandgap and the passband where the band-edge effect is formed, as shown in the figure. At the resonance frequency, the maximum output voltage of the 1st oscillator is 49 V. The primary distinction between B-mode and A-mode is that the center frequency of the local resonance bandgap is higher in B-mode, resulting in a higher power generation frequency band in B-mode than in A-mode.

Here, the total output power frequency response curve of the 1st–6th oscillators of the improved piezoelectric metamaterial beam is shown in Fig. 63a, b, which is further analyzed from the perspective of total power and summed for the above 1st–6th oscillators. Firstly, for A-mode, vibration energy harvesting is achieved in the frequency domain from 625 to 665 Hz, with a maximum value of 51.6 mW at the resonant frequency of 646 Hz, and the passband that generates the band-edge effect also shows large output power values, such as 19.3 mW (631 Hz), 7.7 mW (639 Hz), and 7.1 mW (662 Hz). Similarly, for B-mode, vibration energy harvesting is achieved in the frequency domain from 890 to 940 Hz, reaching 40 mW at the resonant frequency of 912 Hz, with larger output power values of 18.8 mW (902 Hz) and 36.2 mW (928 Hz) in the passband of the band-edge, respectively. Through the above analysis, it is obvious that the improved piezoelectric metamaterial

structure can obtain better power generation performance in both the local resonance bandgap and the passband where the band-edge effect is generated. Therefore, this structure not only broadens the bending wave bandgap action range, but also realizes the power generation effect over a wide frequency range.

3 Finite element analysis

In this section, the multi-physics field coupling software Comsol Multiphysics is used to simulate and verify the dual functions of vibration reduction and power generation of the improved piezoelectric metamaterial beam.

The simulation environment settings are as follows (see Table 4):

The structural and material parameters of the simulation model as well as the circuit component parameters are consistent with the theoretical analysis part.

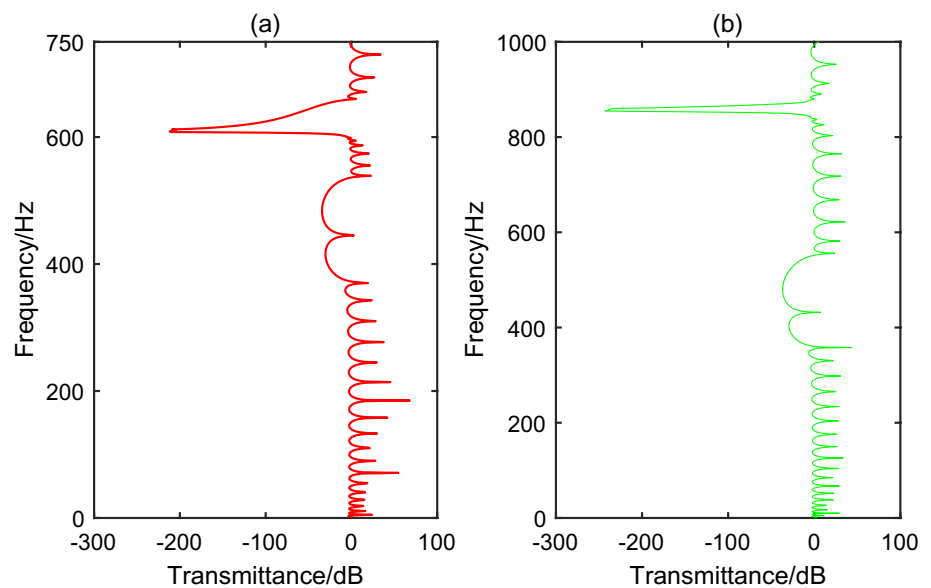
The finite element simulation is carried out for the vibration transmission characteristics of the improved piezoelectric metamaterial beam. Figure 7 depicts the acquired vibration transmission frequency response curve. It should be noticed that the vertical coordinates in the figures are not the same.

From the finite element calculation results in Fig. 7a, b, it can be seen that the bending vibration transmission curves show two bending vibration bandgap structures in the frequency domains of 1–750 Hz and 1–1000 Hz, respectively, the Bragg bandgap and the local resonance bandgap. Comparing the vibration transmission curves of the theoretical analysis and the finite element simulation analysis, it can be seen that there are some differences in the positions and attenuation amounts of the two bandgaps, but the curve trends are generally consistent. On the one hand, these errors come from the difference

Table 4 Finite element simulation analysis environment settings

Items	A-mode	B-mode
Layers m	2	2
Spatial dimension	2D	2D
Physical field	Solid Mechanics—Piezoelectric Devices—Circuits	Solid Mechanics—Piezoelectric Devices—Circuits
Research type	Frequency domain analysis	Frequency domain analysis
Total number of periods	20 periods	20 periods
Loading method	The displacement amplitude of the left-hand end face is 0.01 mm	The displacement amplitude of the left-hand end face is 0.01 mm
Frequency domain	1–750 Hz	1–1000 Hz
Polarization direction	Opposite direction of polarization	Opposite direction of polarization
Piezoelectric bimorph connection type	Parallel connection	Parallel connection
Circuits	L – R parallel connection	L – R parallel connection

Fig. 7 Finite element results of the bending vibration transmission curve of the improved piezoelectric metamaterial beam: **a** A-mode, **b** B-mode



between the theoretical and simulation models. On the other hand, the reason is that the capacitance value of the piezoelectric patch derived from the theoretical analysis is the intrinsic capacitance under constant strain, whereas the actual intrinsic capacitance of the piezoelectric patch is a dynamic value affected by boundary conditions and deformation, and its value is between the intrinsic capacitance of constant strain and constant stress. So there is also a certain deviation between the constant strain capacitance value and the actual value. Because of the aforementioned reasons, the center frequency of the vibration bandgap in the finite element calculation is lower than the theoretical analysis result.

In the finite element simulation environment, the output voltages of 20 pairs of improved piezoelectric oscillators in A-mode and B-mode are calculated respectively, and the output voltages of the 1st–6th pairs of piezoelectric oscillators are also listed, as shown in Fig. 8. It can be found that there are large output voltages in the bandgap of the local resonance and the passband of the band-edge. The power generation performance in the local resonance bandgap is primarily reflected by the oscillators close to the source, as demonstrated by the 1st oscillator's maximum output voltage of 80 V (A-mode) and 64 V (B-mode) at the resonant frequency, respectively; whereas the power generation performance in the passband of the band-edge is primarily reflected by the 1st–6th oscillators. Comparing Figs. 6 and 8, the trend of the output voltage frequency response curve of each oscillator matches with the theoretical analysis except for a slight deviation of the bandgap position and voltage peak value. The deviation of the bandgap position has been analyzed in the previous and will not be repeated here.

4 Impedance matching requirements comparison

The theoretical analysis shows that the improved piezoelectric metamaterial can significantly reduce the resonant frequency of the local oscillator to the original $1/m$ (A-mode) or $1/\sqrt{m}$ (B-mode) compared to the conventional piezoelectric metamaterial for the same electrical parameters. In addition, the A-mode exhibits lower frequency dual-functional performance compared to the multilayer structure of the B-mode. In this section, we focus on A-mode as the research object to analyze and discuss the demand for dual-functional performance on impedance matching in order to obtain the influence law of impedance parameters on vibration suppression performance and energy harvesting performance.

Firstly, the requirements for impedance matching to the vibration suppression performance of the improved piezoelectric metamaterial beams are discussed and analyzed. Figure 9 shows the variation of the transmission characteristics of the improved piezoelectric metamaterial beam (20 periods) with frequency and impedance parameters in the 620–670 Hz frequency domain. It can be found from Fig. 9c that the attenuation range of the bending vibration is mainly concentrated in 635–660 Hz, with the best attenuation effect is achieved at the resonant frequency (646 Hz). When the load resistance value is small, the attenuation impact in the bandgap is not significant, such as $R = 1 \text{ k}\Omega$, $\tau = -2 \text{ dB}$. This is because when $R \rightarrow 0$, the load circuit tends to be short-circuited, the resonant shunt circuit fails, and the flexural wave can propagate without attenuation in the metamaterial beam structure under the condition of disregarding the damping loss. As the load resistance increases, the transmission curve at the resonant frequency shows a monotonically

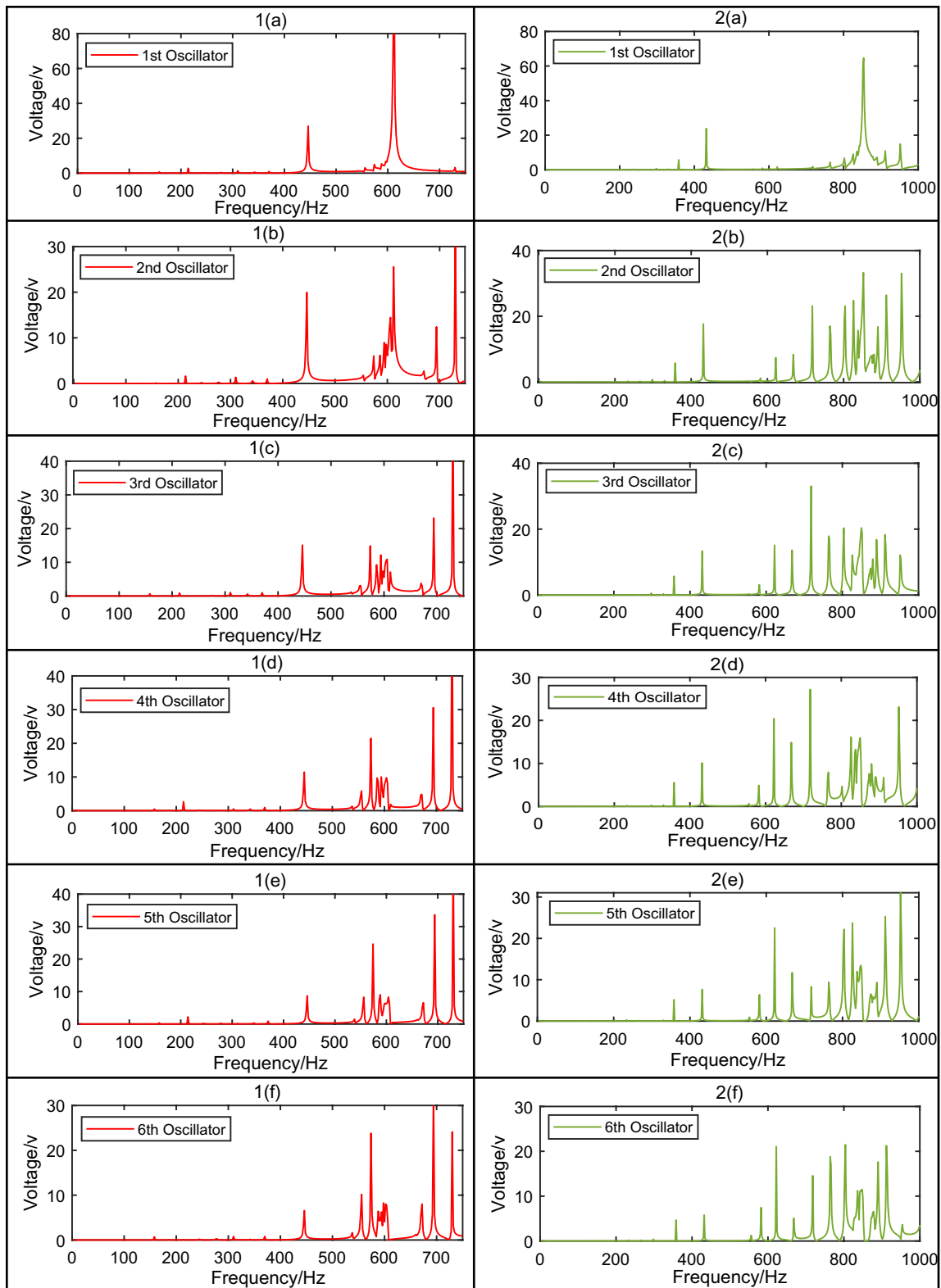


Fig. 8 Finite element results of the output voltage of the 1st–6th oscillators under the bending vibration of the improved piezoelectric metamaterial beam: **1a–1f** A-mode, **2a–2f** B-mode

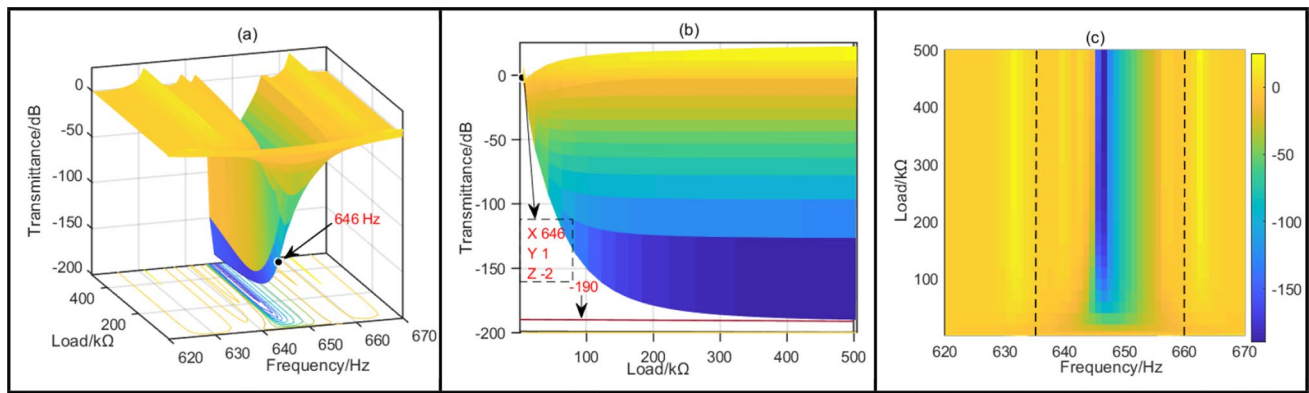


Fig. 9 Optimal transmittance of the improved piezoelectric metamaterial beam versus load resistance and frequency: **a** axonometric view, **b** right view, **c** top view

decreasing trend, i.e., the maximum attenuation in the bandgap gradually increases, and the slope of the transmission curve also shows a decreasing trend; when the load resistance increases to 500 kΩ, the slope of the transmission curve tends to 0, i.e., the attenuation tends to a stable state. In addition, the attenuation bandwidth of the bandgap shows a slow decreasing trend with the growth of the load resistance. The above phenomenon can be explained by the energy band theory. When the load resistance $R \rightarrow \infty$, the load circuit tends to be open-circuit state, and the total impedance of the shunt circuit tends to be Ls ; and from the energy band theory analysis in the second section, it is known that before the introduction of the energy harvesting load circuit (corresponding to the open-circuit state of the load circuit) the electromagnetic resonant bandgap is narrow, and the attenuation at the resonant frequency reaches the maximum; and after the introduction of the energy harvesting external load circuit (corresponding to between the open-circuit and short-circuit states), the improved piezoelectric metamaterial beam exhibits a certain attenuation performance in the pass-band at the band-edge of the local resonance bandgap, which is equivalent to expanding the scope of the local resonant bandgap while reducing the maximum attenuation within the bandgap. Thus the above phenomena arise in consistent with the energy band theory.

Since the power generation performance of the improved piezoelectric metamaterial beam is mainly concentrated in the local resonance bandgap and the passband where generates the band-edge effect. Here, the analysis focuses on the specific connection between the power generation performance and impedance matching in the above bands. The analysis is mainly carried out in terms of both individual oscillator unit and integral beams.

Firstly, we discuss and analyze the impedance influence law of different oscillators at different frequencies. Figure 10a–f lists the relationship between the output power of the 1st–6th oscillators and impedance and frequency. As

shown in the figure, for the power generation performance in the bandgap is mainly reflected in the oscillators close to the source, the reason is attributed to the inherent property of the local resonance bandgap of the metamaterial. The mechanical energy in the local resonance bandgap frequency range will often be localized in the local oscillator structure, and for the finite structure, most of the energy will be absorbed by the oscillators near the source, so that the output power of the oscillators near the source at the resonant frequency are higher. The maximum output power in the bandgap of the 1st–6th oscillator is 55.9 mW, 7.9 mW, 3.6 mW, 2.4 mW, 1.74 mW, and 1.44 mW, respectively. Therefore the 1st oscillator shows the most excellent power generation performance. Taking the 1st oscillator as an example, the influence of impedance parameters on the power generation performance of the oscillator is analyzed. When the load resistance is small, the power generation effect in the bandgap is not significant, such as $R = 1\text{ k}\Omega$ and $P = 0.47\text{ mW}$. The main reason is that when $R \rightarrow 0$, the load circuit tends to be short-circuited and the resonant shunt circuit fails, so the output power tends to be 0. When the R gradually increases, the output power curve at the resonant frequency initially shows a monotonic increasing trend; however, when the resistance value of the load resistance increases to 200 kΩ, the slope of the output power curve is 0 and the output power reaches the extreme point, the corresponding power value (55.9 mW) is called the optimal output power P_{opt} , and the corresponding impedance value (200 kΩ) is called the optimal impedance R_{opt} . When the resistance value of load resistance is greater than R_{opt} , the output power curve at resonant frequency shows a monotonic decreasing trend; when $R \rightarrow \infty$, the load circuit tends to open-circuit state, similar to the short-circuit state, the output power will also tend to 0. The 2nd–6th oscillators exhibit a similar pattern of variation within the bandgap, with corresponding the optimal impedances of 80 kΩ, 120 kΩ, 220 kΩ, 260 kΩ, and 340 kΩ, respectively. Therefore, the impedance matching

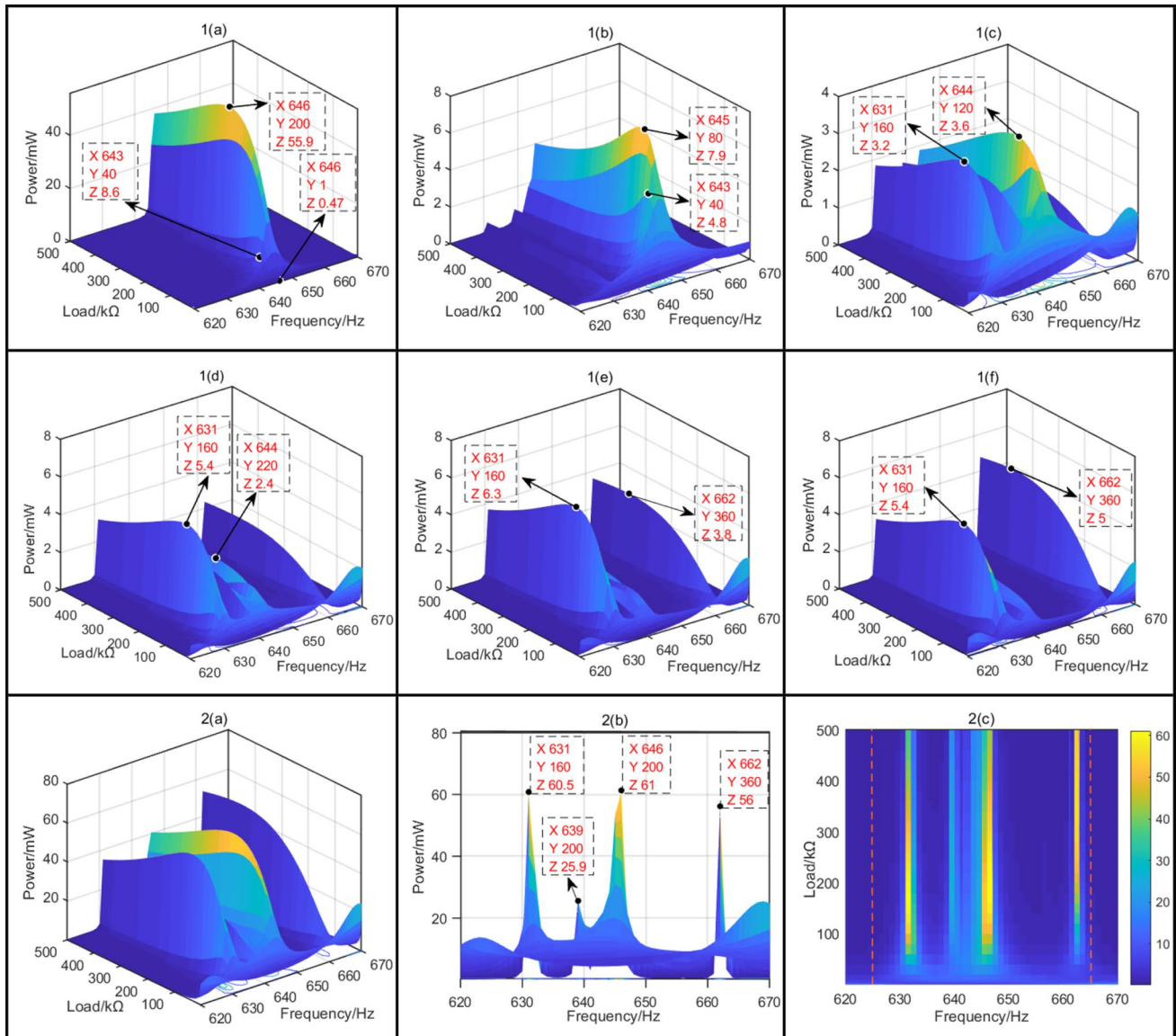


Fig. 10 The 1st–6th oscillators output power of the improved piezoelectric metamaterial beam versus load resistance and frequency: **1a** the 1st oscillator, **1b** the 2nd oscillator, **1c** the 3rd oscillator, **1d** the 4th oscillator, **1e** the 5th oscillator, **1f** the 6th oscillator. Optimal

power of the improved piezoelectric metamaterial beam versus load resistance and frequency: **2a** axonometric view, **2b** right view, **2c** top view

required for optimal power generation performance within the bandgap differs amongst oscillators. Therefore, to make the oscillators near the source can play the optimal power generation effect within the bandgap, it is necessary to connect each oscillator with the corresponding optimal load resistance. Unlike the power generation performance in the bandgap, the passband power generation performance for the band-edge effect is reflected in all oscillators. Mainly due to the influence of the energy harvesting external load circuit on the vibration suppression of the original system, the energy of the band-edge effect mode peak is absorbed by the piezoelectric oscillator and converted into electrical output.

The maximum output power and corresponding impedance of the 1st–6th oscillators are 8.6 mW (40 kΩ), 4.8 mW (40 kΩ), 3.2 mW (160 kΩ), 5.4 mW (160 kΩ), 6.3 mW (160 kΩ), and 5.4 mW (160 kΩ), respectively. It can be found that the maximum output power of each oscillator in the band-edge is significantly lower than the maximum output power of the 1st oscillator at the resonant frequency, but unlike the monotonically decreasing maximum output power with the increase of the number of oscillator stages in the bandgap, the maximum output power values of all oscillators in the band-edge range are relatively more balanced.

Next, in order to characterize the effect of impedance parameters on the power generation performance of the integral beams, the output power of all the oscillators of the 20-period piezoelectric metamaterial beam is summed to obtain the relationship between the total output power and impedance and frequency, as shown in Fig. 10 2a–c. The vibration energy harvesting is achieved throughout the frequency domain of 625–665 Hz, so the improved piezoelectric metamaterial beam structure exhibits a broad frequency power generation effect. Among them, the optimal output power of 61 mW is obtained at the resonant frequency within the bandgap (646 Hz), corresponding to an impedance value of 200 kΩ; and the excellent power generation performance is also achieved in the passband where the band-edge effect is generated, such as 60.5 mW (631 Hz, 160 kΩ), 25.9 mW (639 Hz, 200 kΩ), 56 mW (662 Hz, 360 kΩ), etc. Therefore, similar to the results of the individual oscillator analysis, the impedance matching relationship required for energy harvesting performance and vibration suppression performance is not the same. Therefore, the design and application must be comprehensively considered.

Based on the influence law of impedance parameters on the dual-functional performance of the improved piezoelectric metamaterial beam, if we plan to take the optimal energy harvesting performance within the bandgap as the main goal to select the impedance value [e.g., the optimal impedance value corresponding to 200 kΩ at the resonant frequency (646 Hz)], the dual-functional frequency response calculation of the improved piezoelectric metamaterial beam is carried out on this basis. The frequency response curves of vibration transmission and output power are obtained as shown in Fig. 11, respectively. It can be found that although the impedance matching relationship required for energy harvesting performance and vibration suppression performance is different, the vibration beam also shows a more excellent vibration suppression performance (− 180 dB) when the electrical load with the optimal output power (e.g.,

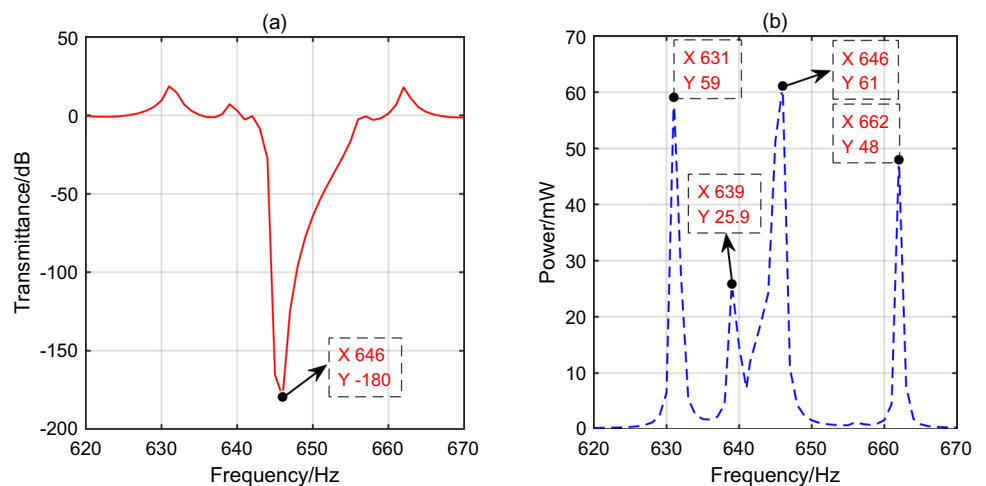
200 kΩ) is selected. In addition, when the impedance value is 200 kΩ, the band-edge also shows a high output power and produces a broadband power generation effect.

5 Conclusions

In this paper, an improved piezoelectric metamaterial beam model is constructed to achieve the dual functions of low-frequency vibration suppression and energy harvesting simultaneously. The energy band structure of an infinite-length model and the vibration transmission characteristics of a finite-length model are analyzed. Meanwhile, the energy harvesting performance of the local resonance bandgap and the band-edge effect frequency band are thoroughly discussed. Finite element simulation analysis is used to verify the correctness of the theoretical analysis. A comparative analysis of impedance matching is carried out for the dual-functional performance of the improved piezoelectric metamaterial beam. The main conclusions are as follows:

- Compared to the conventional piezoelectric metamaterial beam, the improved piezoelectric metamaterial beam generates a lower frequency bandgap with the same electrical parameters, not only improving the vibration suppression in the low frequency band, but also extending the application range of energy harvesting to a lower frequency band. The resonant frequency of the local oscillator is depending on the number of layers (m) and stacking mode, which is corresponding to $1/m$ (A-mode) or $1/\sqrt{m}$ (B-mode) of the conventional piezoelectric metamaterials. Furthermore, the influence law of inductance parameters indicates that the improved piezoelectric metamaterials can effectively overcome the disadvantage of reducing the center frequency of the local resonant bandgap by using large inductive elements in conventional piezoelectric metamaterials.

Fig. 11 The frequency response curve of the improved piezoelectric metamaterial beam under the electric load corresponding to the optimal output power **a** frequency response curve of vibration transmission; **b** frequency response curve of total output power



- The improved piezoelectric metamaterial beam structure with the introduction of an external load circuit for energy harvesting has a significant suppression effect on the metamaterial band-edge effect, especially in the lower band-edge resonance dense frequency band, which in turn broadens the action range of the local resonance bandgap, while decreasing the maximum attenuation within the bandgap. Furthermore, the improved piezoelectric metamaterial beam exhibits significant power generation performance in the local resonance bandgap and the passband where the band-edge effect occurs, achieving a broadband power generation effect.
- Vibration suppression performance and energy harvesting performance have different impedance requirements and necessitate different impedance matching schemes to achieve the optimal vibration suppression performance and energy harvesting performance. However, when the electrical load with the optimal output power in the bandgap is selected as the design basis, not only can a broadband power generation capability be realized in the bandgap and the passband that generates the band-edge effect, but the vibration beam also exhibits relatively excellent vibration suppression performance.

Acknowledgements This work was funded by the project (grant number 51875112) supported by the National Natural Science Foundation of China, the project (grant number 145109203) supported by the Fundamental Research Funds of Education Department of Heilongjiang Provincial.

References

1. Y.M. Liu, X. Zhang, Metamaterials: a new frontier of science and technology. *Chem. Soc. Rev.* **40**, 2494–2507 (2011)
2. F. Lemoult, N. Kaina, M. Fink, Wave propagation control at the deep subwavelength scale in metamaterials. *Nat. Phys.* **9**, 55–60 (2013)
3. N. Kaina, F. Lemoult, M. Fink, G. Lerosey, Negative refractive index and acoustic superlens from multiple scattering in single negative metamaterials. *Nature* **525**, 77–81 (2015)
4. M.I. Hossain, M.R.I. Faruque, M.T. Islam, Double-negative metamaterial for mobile phone application. *Appl. Phys. A-Mater. Sci. Process.* **123**, 30 (2017)
5. L. Ji, V.V. Varadan, Negative refractive index and negative refraction of waves in lossy metamaterials. *Electron. Lett.* **52**, 260–261 (2016)
6. Z. Chen, B. Guo, Y. Yang et al., Metamaterials-based enhanced energy harvesting: a review. *Phys. B Phys. Condensed Matter* **438**, 1–8 (2014)
7. G. Hu, L. Tang, J. Liang et al., Acoustic-elastic metamaterials and phononic crystals for energy harvesting: a review. *Smart Mater. Struct.* **30**, 085025 (2021)
8. Y. Jian, L. Tang, G. Hu et al., Design of graded piezoelectric metamaterial beam with spatial variation of electrodes. *Int. J. Mech. Sci.* **218**, 107068 (2022)
9. A. Salakhitdinov, E. Ibragimova, M. Salakhitdinova, Negative induced absorption and negative index of refraction for iron doped potash-alumina-borate glasses subjected to thermal-radiation treatment. *Appl. Phys. A-Mater. Sci. Process.* **124**, 187 (2018)
10. W. Xingguo, S. Haisheng, Z. Lei, Vibration and acoustic insulation properties of generalized phononic crystals. *Eur. Phys. J. Appl. Phys.* **94**, 30902 (2021)
11. Qi. Xiaoqiao, Li. Tuan-jie, Z. Jia-long et al., Band gap structures for 2D phononic crystals with composite scatterer. *Appl. Phys. A-Mater. Sci. Process.* **124**, 364 (2018)
12. W. Chaohui, W. Shuai, G. Zhiwei et al., Effect evaluation of road piezoelectric micro-energy collection-storage system based on laboratory and on-site tests. *Appl. Energy* **287**, 116581 (2021)
13. Oh. Yongkeun, K. Dae-Sung, E. Youngkee et al., Flexible energy harvester with piezoelectric and thermoelectric hybrid mechanisms for sustainable harvesting. *Int. J. Precis. Eng. Manuf.-Green Technol.* **6**, 691–689 (2019)
14. Q. Yi, W. Tiantian, Z. Yue et al., Simulation and experiment on bridge-shaped nonlinear piezoelectric vibration energy harvester. *Smart Mater. Struct.* **28**, 045015 (2019)
15. Z. Yu, C.Y. Zhang, S.Y. Zhang, Simulation analysis and optimization design for wide band piezoelectric oscillator of energy harvesting device. *J. Mech. Sci. Technol.* **34**, 2745–2750 (2020)
16. J.D. Hobeck, D.J. Inman, Simultaneous passive broadband vibration suppression and energy harvesting with multifunctional metastructures. In: *Tribute Conference Honoring Daniel Inman*. **10172**, 101720K (2017)
17. Y. Li, E. Baker, T. Reissman et al., Design of mechanical metamaterials for simultaneous vibration isolation and energy harvesting. *Appl. Phys. Lett.* **111**, 251903 (2017)
18. Hu. Guobiao, L. Tang, A. Banerjee et al., Metastructure with piezoelectric element for simultaneous vibration suppression and energy harvesting. *J. Vib. Acoust.* **139**, 011012 (2017)
19. Hu. Guobiao, L. Tang, R. Das, Internally coupled metamaterial beam for simultaneous vibration suppression and low frequency energy harvesting. *J. Appl. Phys.* **123**, 055107 (2018)
20. X. Zhang, H. Zhang, Z. Chen et al., Simultaneous realization of large sound insulation and efficient energy harvesting with acoustic metamaterial. *Smart Mater. Struct.* **27**, 105018 (2018)
21. Su. Chen Jungsan, C.Y. Weijiun et al., A metamaterial structure capable of wave attenuation and concurrent energy harvesting. *J. Intell. Mater. Syst. Struct.* **30**, 2973–2981 (2019)
22. A. Dwivedi, A. Banerjee, B. Bhattachary, Simultaneous energy harvesting and vibration attenuation in piezo-embedded negative stiffness metamaterial. *J. Intell. Mater. Syst. Struct.* **31**, 1076–1090 (2020)
23. W. Anigbogu, H. Bardaweel, A metamaterial-inspired structure for simultaneous vibration attenuation and energy harvesting. *Shock Vib.* **2020**, 4063025 (2020)
24. Y.-W. Zhang, C. Su, Z.-Y. Ni, A multifunctional lattice sandwich structure with energy harvesting and nonlinear vibration control. *Compos. Struct.* **221**, 110875 (2019)
25. D. Cao, X. Guo, Hu. Wenhua, A novel low-frequency broadband piezoelectric energy harvester combined with a negative stiffness vibration isolator. *J. Intell. Mater. Syst. Struct.* **30**, 1105–1114 (2019)
26. M. Bukhari, O. Barry, Simultaneous energy harvesting and vibration control in a nonlinear metastructure: a spectro-spatial analysis. *J. Sound Vib.* **473**, 115215 (2020)
27. Lu. Z-Q, L. Zhao, H. Ding et al., A dual-functional metamaterial for integrated vibration isolation and energy harvesting. *J. Sound Vib.* **509**, 116251 (2021)
28. C. Sugino, A. Erturk, Graded multifunctional piezoelectric metastructures for wideband vibration attenuation and energy harvesting. *Smart Mater. Struct.* **30**, 015029 (2021)
29. C. Sugino, A. Erturk, Analysis of multifunctional piezoelectric metastructures for low-frequency bandgap formation and energy harvesting. *J. Phys. D Appl. Phys.* **51**, 215103 (2018)

30. C. Sugino, S. Leadenham, M. Ruzzene, A. Erturk, An investigation of electroelastic bandgap formation in locally resonant piezoelectric metastructures. *Smart Mater. Struct.* **26**, 055029 (2017)
31. X. Wang, L. Wang, H. Shu, Research on dual-functional characteristics of piezoelectric metamaterial beams for vibration reduction and power generation. *AIP Adv.* **12**, 025326 (2022)
32. H. Ding, W. Chen, *Three Dimensional Problems of Piezoelectricity* (Nova Science Publishers, New York, 2001)
33. S. Chen, J. When, G. Wang et al., Improved modeling of rods with periodic arrays of shunted piezoelectric patches. *J. Intell. Mater. Syst. Struct.* **23**, 1613–1621 (2012)

Publisher's Note Springer Nature remains neutral with regard to jurisdictional claims in published maps and institutional affiliations.

Springer Nature or its licensor holds exclusive rights to this article under a publishing agreement with the author(s) or other rightsholder(s); author self-archiving of the accepted manuscript version of this article is solely governed by the terms of such publishing agreement and applicable law.